PRIMUS: GALAXY ENVIRONMENT ON THE QUIESCENT FRACTION EVOLUTION AT $Z < 1$

ChangHoon Hahn, Michael Blanton, Alison Coil, Richard Cool, Daniel Eisenstein, John Moustakas, Ken Wong, Guangtun Zhu

Draft version May 29, 2014

ABSTRACT

We investigate the effects of galaxy environment on the evolution of the quiescent fraction ($f_{\rm Q}$) from $z = 0.8$ to 0.0 using spectroscopic redshifts and multi-wavelength imaging data from PRism MUlti-object Survey (PRIMUS) and the Sloan Digitial Sky Survey (SDSS). Our stellar mass limited galaxy sample consists of ~ 40000 PRIMUS galaxies within $z = 0.2 - 0.8$ and ~ 130000 SDSS galaxies within $z = 0.0375 - 0.145$. We classify the galaxies as quiescent or star-forming, based on an evolving specific star formation cut, and as low or high density environments, based on fixed cylindrical aperture environment measurements on a volume-limited *Environment Definition Population* (from PRIMUS and SDSS). We examine the stellar mass function (SMF) evolution for each of our subsamples of quiescent and star-forming galaxies in low and high density environments. We find, from the $f_{\rm Q}(\mathcal{M}_*)$ computed from these SMFs, that in both low and high density environments the quiescent fraction increases with cosmic time over the probed redshift range. Moreover, the difference between the quiescent fraction in low and high density environments remains constant throughout the redshift range. These results suggest that the evolution of the quiescent fraction is independent of environment and provide constraints on quenching mechanisms in high density environments such as groups and clusters.

1. INTRODUCTION

Galaxies, in their detailed properties, carry the imprints of their surroundings, with a strong dependence of the quiescent fraction of galaxies on their local environment (e.g. Hubble 1936; Oemler 1974; Dressler 1980; Hermit et al. 1996; Guzzo et al. 1997; for a recent review see Blanton & Moustakas 2009). The strength of this dependence is itself a strongly decreasing function of galaxy stellar mass; at the extreme, the lowest masses ($< 10^9$ $M_\odot$) galaxies are quenched only in dense regions, and never in isolation (Geha et al. 2012). These effects vary with redshift at least in the densest clusters, as observed in the changing fraction of late-type spirals relative to the field found in studies of the morphology-density relation (Dressler 1984; Desai et al. 2007). Clearly understanding the properties of galaxies in the present-day universe requires a careful investigation of the role of environment, and how that role changes over time.

Nevertheless, the evolution of the role of environment is a relatively subtle effect and difficult to study. Although history of galaxies prior to $z \sim 1$ appears to have been one of rapid assembly, since that time the galaxy population has continued to evolve, but less dramatically. Although there are detectable changes in the population, the major classes of galaxies existed at $z \sim 1$, in roughly the same relative numbers as today (Bundy et al. 2006; Borch et al. 2006; Taylor et al. 2009; Moustakas et al. 2013a. Furthermore, at those redshifts we can also detect the dependence of galaxy properties on environment, with lower star-formation rate early-type galaxies populating the denser regions (Cooper et al. 2008; Patel et al. 2009; Kovač et al. 2010).

The most dramatic change in galaxy properties during the past eight billion years has been a remarkable decline in the star-formation rate of galaxies in the Universe (Hopkins & Beacom 2006). This decline appears dominated by decreases in the rates of star-formation of individual galaxies (Noeske et al. (2007)). There is evidence that a large fraction of the decline associated with strongly infrared-emitting starbursts (Bell et al. 2005; Magnelli et al. 2009). The decline does not appear to be due to the quenching of a large fractions of the star-forming population, as reflected in observations of the stellar mass function of quiescent and star-forming galaxies (Blanton et al. (2006),Bundy et al. 2006; Borch et al. 2006; Moustakas et al. 2013a). These findings leave little room for the participation of environmentally-driven quenching in the global census of star-formation. As Cooper et al. (2008) and others have pointed out, because the environmental dependence of total star-formation rates at fixed redshift is relatively small, environmentally effects are unlikely to cause the overall star-formation rate decline.

Thus, the impact of environment on galaxy formation has to be interpreted on top of the background of this overall decline affecting galaxies in all environments. The most straightforward investigation of would directly determine the star-forming properties of galaxies as a function of environment, stellar mass and redshift in a single, consistently analyzed data set. This analysis can reveal how galaxies are quenched in the universe over time, quantitatively establish the contribution of environmental effects to the overall trends, and reveal whether those trends happen equally in all environments. However, such an analysis has not been done previously due to the lack of sufficiently large samples. In this paper, we apply this approach using the Prism Multi-object Survey (PRIMUS; Coil et al. (2011), Cool et al. (2013)), the largest available redshift survey covering the epochs between $0 < z < 1$.

2. SAMPLE SELECTION

In this paper we are interested in measuring the evolution of the quiescent fraction over a wide range of redshifts and in different galaxy environments. In order construct a sample with redshift depth and robust enough redshift values to measure galaxy environment, we use galaxies at intermediate redshifts from PRIMUS. Additionally we supplement our sample with galaxies at low redshift ($z \sim 0.1$) from SDSS.

We begin with a brief summary of the PRIMUS data in Section 2.1 followed by a summary of the SDSS data in Section 2.2. Then in Section 2.3 we use this data to define the stellar mass complete target galaxy population. Afterwards, in Section 2.4, we classify these target galaxies as quiescent or active star-forming galaxies. For each galaxy we obtain the environment using a volume-limited *Environment Defining Population* in Section 2.5. Finally in Section 2.6, we correct the galaxy sample and its environment measurements for the edge effects of the surveys.

2.1. *PRIMUS*

For galaxies at intermediate redshifts we use multi-wavelength imaging and spectroscopic redshifts data of PRIMUS, which is a faint galaxy survey with precise spectroscopic redshifts ($\sigma_z/(1+z) \approx 0.5\%$) for $\sim 120,000$ galaxies within redshifts $z \approx 0 - 1.2$. The survey was conducted using a IMACS spectrograph on a Magellan I Baade 6.5 m telescope with a slitmask and low dispersion prism. For further details on the PRIMUS observation methods, including survey design, targeting, and data summary, we refer readers to the survey papers: Coil et al. (2011) and Cool et al. (2013).

As done in Moustakas et al. (2013b), we only use fields targeted by PRIMUS with *GALEX* and *Spitzer*/IRAC imaging. This restricts us to five fields. Four of these fields are a part of the *Spitzer* Wide-area Infrared Extragalactic Survey (SWIRE[1]): the European Large Area ISO Survey - South 1 field (ELAIS-S1[2]), the Chanddra Deep Field South SWIRE field (CDFS), and the XMM Large Scale Structure Survey field (XMM-LSS). The XMM-LSS consists of two separate but spatially adjacent fields: the Subaru/XMM-Newton DEEP Survey fied (XMM-SXDSS[3]) and the Canadian-France-Hawaii Telescope Legacy Survey field (XMM-CFHTLS[4]). In addition to the SWIRE fields we also include the COSMOS[5] field for a total of five fields.

In all of the PRIMUS target fields we have near-UV (NUV) and far-UV (FUV) measurements from the *GALEX* Deep Imaging Survey (DIS; Martin et al. (2005); Morrissey et al. (2005)). To minimize contamination from neighboring sources, we use a Bayesian photometric code EM_{PHOT} (based on expectation maximization algorithm of Guillaume et al. (2006)). Furthermore, we use ground-based optical and *Spitzer*/IRAC mid-infrared photometric catalogs in each of the fields to obtain integrated fluxes in all photometric bands. To summarize, the general strategy employed is to use a circular aperture photometry to constrain the shape of the SED and

[1] http://swire.ipac.caltech.edu/swire/swire.html
[2] http://dipastro.pd.astro.it/esis
[3] http://www.naoj.org/cience/SubaruProject/SDS
[4] http://www.cfht.hawaii.edu/Science/CFHLS
[5] http://cosmos.astro.caltech.edu

Survey	Redshift (z)	Density	Quiescent	Star-forming
SDSS	$0.0375 - 0.145$	High	5470	4501
		Mid	3614	4438
		Low	5419	8927
PRIMUS	$0.2 - 0.4$	High	322	583
		Mid	177	403
		Low	768	2516
PRIMUS	$0.4 - 0.6$	High	350	675
		Mid	195	405
		Low	871	2385
PRIMUS	$0.6 - 0.8$	High	347	430
		Mid	186	327
		Low	833	1847
PRIMUS	$0.8 - 1.0$	High	136	232
		Mid	94	163
		Low	373	810

then fixing the overall normalization to a estimate of the total magnitude in the detection band. Moustakas et al. (2013b) provides a detailed description of the calculation for each of our target fields.

From the spectroscopic redshift and photometry described above, we use `iSEDfit` to determine stellar masses, star formation rates (SFRs) and other physical properties in a simplified Bayesian framework. `iSEDfit`, which we will only briefly mention in this paper is discussed in detail in Appendix A. of Moustakas et al. (2013b). The code uses the redshift and the observed photometry of the galaxies to determine the statistical likelihood of a large ensemble of generated model SEDs. These generated model SEDs depend on population synthesis models and prior parameters. In order to derive our fiducial stellar masses and star formation rates, we use the Flexible Stellar Population Synthesis (FSPS) models (Conroy & Gunn (2010)) based on the Chabrier (2003) IMF. Other prior parameters are listed in Section 4.1 of Moustakas et al. (2013b). The photometric bands we use for the fitting in our PRIMUS data are the *GALEX* FUV and NUV, the two shortest IRAC bands at 3.6 and $4.5\mu m$, and the five optical bands (in the COSMOS field, we fit seven optical bands and near-infrared bands, see Section 2.3 of Moustakas et al. (2013b)). For a more detailed description of the data used in this paper, we refer readers to Moustakas et al. (2013b) Section 2 and Section 4.1.

2.2. *SDSS-GALEX*

For galaxies at low redshifts we use the SDSS Data Release 7 (DR7; Abazajian et al. (2009)). From the SDSS DR7 data, which provides high fidelity *ugriz* photometry and spectroscopic redshift, we specifically use galaxies from the New York University Value-Added Galaxy Catalog that satisfy the main sample criterion and have galaxy extinction corrected Petrosian magnitudes $14.5 < r < 17.6$ and spectroscopic redshifts within
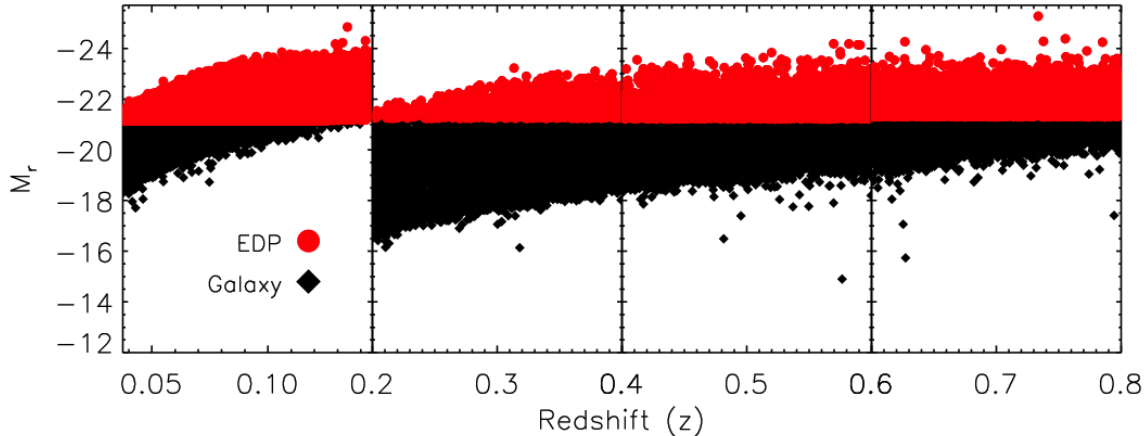
FIG. 1.— Absolute magnitude M_r versus redshift for the target galaxy population (black) with the Environment Defining Population (red) plotted on top. Both samples are divided into redshift bins:$0.0375 - 0.145$, $0.2 - 0.4$, $0.4 - 0.6$, and $0.6 - 0.8$. Stellar mass completeness limits are imposed on the target galaxy population (Section 2.3) while the M_r limits are imposed on the EDP (Section 2.5).

$0.01 < z < 0.2$ (Blanton et al. (2005b)). Within this sample, we select galaxies with medium depth observations from GALEX. This is done by first retrieving the positions of all *GALEX* tiles from GALEX Release 6 with total exposure time greater than 1 ks and then constructing a joint angular selection function of the SDSS-*GALEX* Sample. This results in a final sample of $167,727$ SDSS galaxies with *GALEX* imaging.

For this final sample, we use the MAST/CasJobs[6] interface and a $4''$ diamater search radius to obtain the NUV and FUV photometry. For the optical photometry we use *ugriz* bands (from the SDSS `model` magnitudes) scaled to the *r*-band `cmodel` magnitude. We supplement the above UV and optical photometry with integrated JHK_s magnitudes from the 2MASS Extended Source Catalog (XSC; Jarrett et al. (2000)) and with photometry at 3.4 and 4.6μm from the WISE All-Sky Data Release[7]. Further details on the photometry of the SDSS data used in this paper is provided in Moustakas et al. (2013b) Section 2.4.

To obtain the stellar masses and SFRs for the SDSS data we use `iSEDfit`, as we did for the PRIMUS data in Section 2.1. However, we use twelve photometric bands: *GALEX* FUV and NUV, SDSS *ugriz*, 2MASS JHK_s, and WISE 3.4 and 4.6μm.

2.3. *Target Galaxy Sample*

In this section we will define the target galaxy sample used to compute the SMFs and QFs. The population at $z \sim 0.5$ is derived from PRIMUS data and the population at $z \sim 0.1$ is derived from SDSS-*GALEX* data, both described above. For the intermediate redshift population, we begin with the selection criteria imposed in Moustakas et al. (2013b) for their parent sample. We take the statistically complete *primary* sample from the PRIMUS data (Coil et al. (2011)) and impose magnitude limits on optical selection bands as specified in Moustakas et al. (2013b) Table 1. These limits are in different

[6] http://galex.stsci.edu/casjobs
[7] http://wise2.ipac.caltech.edu/docs/release/allsky

optical selection bands and have distinct values for the five PRIMUS target fields. We then exclude stars and broad-line AGN to only select objects spectroscopically classified as galaxies, with high-quality spectroscopic redshifts ($Q \geq 3$) within the redshift range $0.2 - 0.8$. For each of these objects we assign statistical weights (described in Coil et al. (2011) and Cool et al. (2013)) in order to correct for targeting incompleteness and redshift failures. The statistical weight, w_i, for each galaxy is given by

$$w_i = (f_{\text{target}} \times f_{\text{collision}} \times f_{\text{success}})^{-1}, \qquad (1)$$

Equation (1) in Moustakas et al. (2013b). Then to account for stellar mass incompleteness, we impose derived stellar mass limits to the sample.

Stellar mass completeness limits for a magnitude-limited survey such as PRIMUS is a function of redshift, apparent magnitude limit of the survey, and the typical stellar mass-to-light ratio of galaxies near the flux limit. As done in Moustakas et al. (2013b), we follow Pozzetti et al. (2010) to empirically determine the stellar mass completeness limits. Briefly, for each of the target galaxies we compute $\mathcal{M}_{\text{lim}}$ using $\log \mathcal{M}_{\text{lim}} = \log \mathcal{M} + 0.4(\text{m} - \text{m}_{\text{lim}})$. $\mathcal{M}$ is the stellar mass of the galaxy in $\mathcal{M}_\odot$, $\mathcal{M}_{\text{lim}}$ is the stellar mass of each galaxy if its magnitude was equal to the survey magnitude limit, m is observed apparent magnitude in the selection band, and m_{lim} is the magnitude limit for our five fields mentioned above. We construct a cumulative distribution of $\mathcal{M}_{\text{lim}}$ for the 15% faintest galaxies in $\Delta z = 0.04$ bins. In each of these redshift bins, we calculate the minimum stellar mass that includes 95% of the galaxies. Separately for quiescent and star-forming galaxies, we fit quadratic polynomials to the minimum stellar masses versus redshift (galaxies are classified into star-forming or quiescent in the following section). Finally, we use the polynomials to obtain the minimum stellar masses at the center of redshift bins, $0.2 - 0.4$, $0.4 - 0.6$, and $0.6 - 0.8$, which are then used as PRIMUS stellar mass completeness limits.

For our target galaxy population at low redshift we start with the SDSS-*GALEX* data. We limit our pop-

ulation within the redshift range $0.0375 - 0.145$ due to redshift limits later imposed on the volume-limited Environment Defining Population (Section 2.5). To account for targeting completeness of this sample, we use the statistical weight estimates provided by the NYU-VAGC. Then to account for stellar mass incompleteness, we impose a uniform stellar mass limit of $10^9.8\mathcal{M}_\odot$, a limit determined by the stellar mass-to-light ratio completeness of the NYU-VAGC sample given the redshift limits.

The absolute magnitude (M_r) versus redshift for the target galaxy population (black squares) is plotted in Figure 2.1. The left-most panel corresponds to the target sample derived from the SDSS-$GALEX$ data and the rest correspond to the target sample derived from the PRIMUS data divided in bins with $\Delta z \sim 0.2$.

2.4. *Classifying Quiescent and Star-Forming Galaxies*

With the galaxy sample defined in the previous section, we now classify the galaxies as quiescent or star-forming using an evolving cut based on specific star-formation rate utilized in Moustakas et al. (2013b) Section 3.2. To summarize, this classification method utilizes the star-forming (SF) sequence, which is the correlation between star-formation rate (SFR) and stellar mass in star-forming galaxies observed at least until $z \sim 2$. The PRIMUS sample displays a well-defined SF sequence within the redshift range of our target population. Using the power-law slope for the SF sequence derived by Salim et al. (2007) (SFR $\propto \mathcal{M}^{0.65}$) and the minimum of the quiescent/star-forming bimodality, determined empirically, we obtain the following equation to classify the target galaxies (Equation 2 in Moustakas et al. (2013b)):

$$\log(\mathrm{SFR}_{\min}) = -0.49 + 0.64\log(\mathcal{M} - 10) + 1.07(z - 0.1), \tag{2}$$

where $\mathcal{M}$ is the stellar mass of the galaxy. If the target galaxy SFR and stellar mass place the galaxy above Equation 2 we classify it as star-forming; if below, as quiescent (Moustakas et al. (2013b) Figure 1.).

2.5. *Galaxy Environment*

In addition to the quiescent/star-forming classification, in this section, we measure the environment for our target galaxies. We define the environment of a galaxy as the number of neighboring galaxies contained within a fixed aperture centered around it. We use a fixed aperture environment because, as Muldrew et al. (2012) finds in their comparison of different environment definition using simulations, it provides a better probe of the entire halo in comparison to other environment definitions such as nearest neighbor, which provides a better tracer at inter-halo scales. For our aperture, we use a cylinder of dimensions: $R_{\mathrm{ap}} = 2$ Mpc/h and $H_{\mathrm{ap}} = 25$ Mpc/h. Though spherical apertures are often used in literature (e.g. Croton et al. (2005)), we use a cylindrical aperture in order to account for the PRIMUS redshift errors and redshift space distortions (i.e. "Finger of God" effect). **?** finds that ± 1000 kms^{-1} optimally reduces the effects of redshift space distortions and PRIMUS $\sigma_z \sim 0.0085$ at $z \sim 0.7$, so aperture height of 25 Mpc/h successfully accounts for both of these effects. Furthermore, our choice of cylinder radius was motivated by scale dependence analyses in literature (Blanton et al. (2006), **?**, and Muldrew et al. (2012)), which suggest that galactic proper-

ties such as color and quenched fractions are dependent on halo-scale properties such as host dark matter halo mass. **?**, which uses environment defined by annuli of different radii, find positive correlation for quenched fraction and color on scales < 1 Mpc and anti-correlation on scales > 3 Mpc. Our choice of 2Mpc/h provides sufficient sample size of galaxies in dense environments, for robust statistics, while tracing galactic properties within the halo scale. When we extend our analysis to cylindrical apertures with $R_{\mathrm{ap}} = 1$ Mpc/h, we find that the change in R_{ap} does not significantly change our results (difference in $f_Q < 0.05$).

With proper motivation for the fixed aperture environment definition, we now proceed to measuring the environment for our target galaxies. First, we construct a volume limited *Environment Defining Population* (EDP) with absolute magnitude cut-offs (M_r) at each redshift bin. EDP galaxies within the aperture surrounding each target galaxy are the neighboring galaxies in our definition of environment. The M_r cut-offs for the EDP are selected so that the cumulative number density over M_r at all redshift bins are equal. Not only does this provide a reasonably comparison of the environment measurements at different redshifts but it also seeks to construct an EDP that contains similar galaxy populations throughout our redshift range (i.e. to account for the progenitor bias in our EDP). As Behroozi et al. (2013) and Leja et al. (2013) find in their analysis of the cumulative number density method, the cumulative number density method, though it does not precisely account for the scatter in mass accretion or galaxy-galaxy mergers, provides a reasonable means to compare galaxy populations over a wide range of cosmic time.

In constructing the EDP for the PRIMUS (hereafter PRIMUS EDP) we use the same PRIMUS data as the target galaxies, described in Section 2.3. We restrict the PRIMUS galaxies to $0.2 < z < 0.8$ and divide them into bins of $\Delta z = 0.2$. Before we consider the cumulative number densities in these bins, we first determine M_r limit for the highest redshift bin $(0.6 - 0.8)$ by examining the M_r distribution with bin size $\Delta M_r = 0.25$ and select $M_{r,\mathrm{lim}}$ near the peak of the distribution where bins with $M_r > M_{r,\mathrm{lim}}$ have fewer galaxies than the bin at $M_{r,\mathrm{lim}}$. We choose $M_{r,\mathrm{lim}}(0.6 < z < 0.8)$ to be, conservatively, $M_r = -20.75$. For the other redshift bins, we impose absolute magnitude limits $(M_{r,\mathrm{lim}})$ such that the cumulative number density of the bin ordered by M_r is equal to the cumulative number density of the highest redshift bin. The cumulative number density calculations accounts for the statistical weights of the galaxies (Section 2.1 and 2.2).

For the SDSS-$GALEX$ EDP (hereafter SDSS EDP), we do not use the parent data of the SDSS-$GALEX$ target sample which uses the geometry of the combined angular selection function of the SDSS VAGC and $GALEX$. Instead, since FUV, NUV values are not necessary for EDP, we extend the parent data of the SDSS EDP to the entire SDSS VAGC, including galaxies outside of the $GALEX$ window function. Furthermore, we impose a redshift range of $0.0375 - 0.145$ on the SDSS EDP. This redshift range is due to the lack of faint galaxies at $z \sim 0.2$ and the lack of bright galaxies at $z \sim 0.01$ in the SDSS VAGC data. The lower bound for the redshift range was empirically determined by the bright limit and
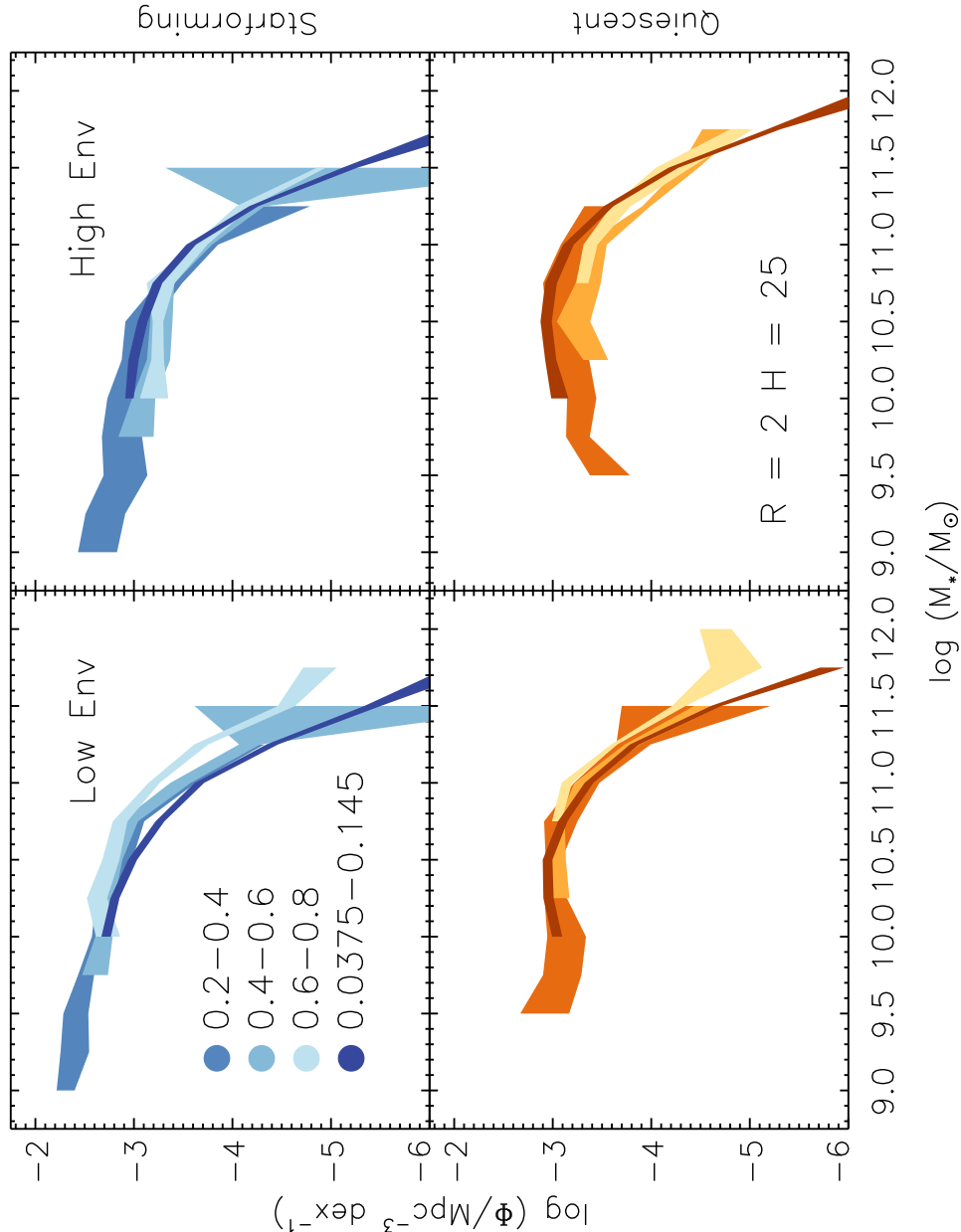
FIG. 2.— Evolution of stellar mass functions of star-forming (top) and quiescent (bottom) target galaxies in low (left) and high (right) environments from redshift range $z = 0 - 0.8$. The environment of each galaxy was calculated using a cylindrical aperture size of $R = 2\,\mathrm{Mpc}$ and $H = 25$ Mpc and classification based on the cut-offs specified in Table 2. The SMFs use mass bins of width $\Delta\log(\mathcal{M}/\mathcal{M}_\odot) = 0.25$. In each panel we use shades of blue (star-forming) and orange (quiescent) to represent the SMF at different redshift, higher redshifts being progressively lighter.

the upper bound by the faint limit of the M_r versus redshift distribution. The same fixed cumulative number density method, described above, is used on this SDSS EDP to equate the cumulative number density of SDSS EDP to the highest redshift bin of the PRIMUS EDP. Ultimately, we get $M_{r,\mathrm{lim}} = -20.57, -20.73, -20.80$ and -20.95 for the redshift bins $0.0375 - 0.145$, $0.2 - 0.4$, $0.4 - 0.6$, $0.6 - 0.8$, respectively. These absolute magnitude limits are illustrated in Figure 2.1, which plots M_r distribution as a function of redshift for the EDP (red) and the target galaxy sample (black).

Finally with the EDP we measure the environment for each of the target sample galaxies by counting the num-

ber of EDP galaxies, n_{env}, with RA, Dec, and redshift within the aperture surrounding it. n_{env} accounts for the statistical weights of the EDP galaxies. More specific details for the dense and sparse environment cut-offs the various apertures are provided in Table 2.

2.6. *Edge Effects*

One of the challenges in obtaining the galaxy environment using a fixed aperture method is accounting for the edges of the survey. For galaxies located near the edge of the survey, part of the fixed aperture encompassing it will lie outside the survey regions. In this case, the n_{env} will only reflect the fraction of the environment within
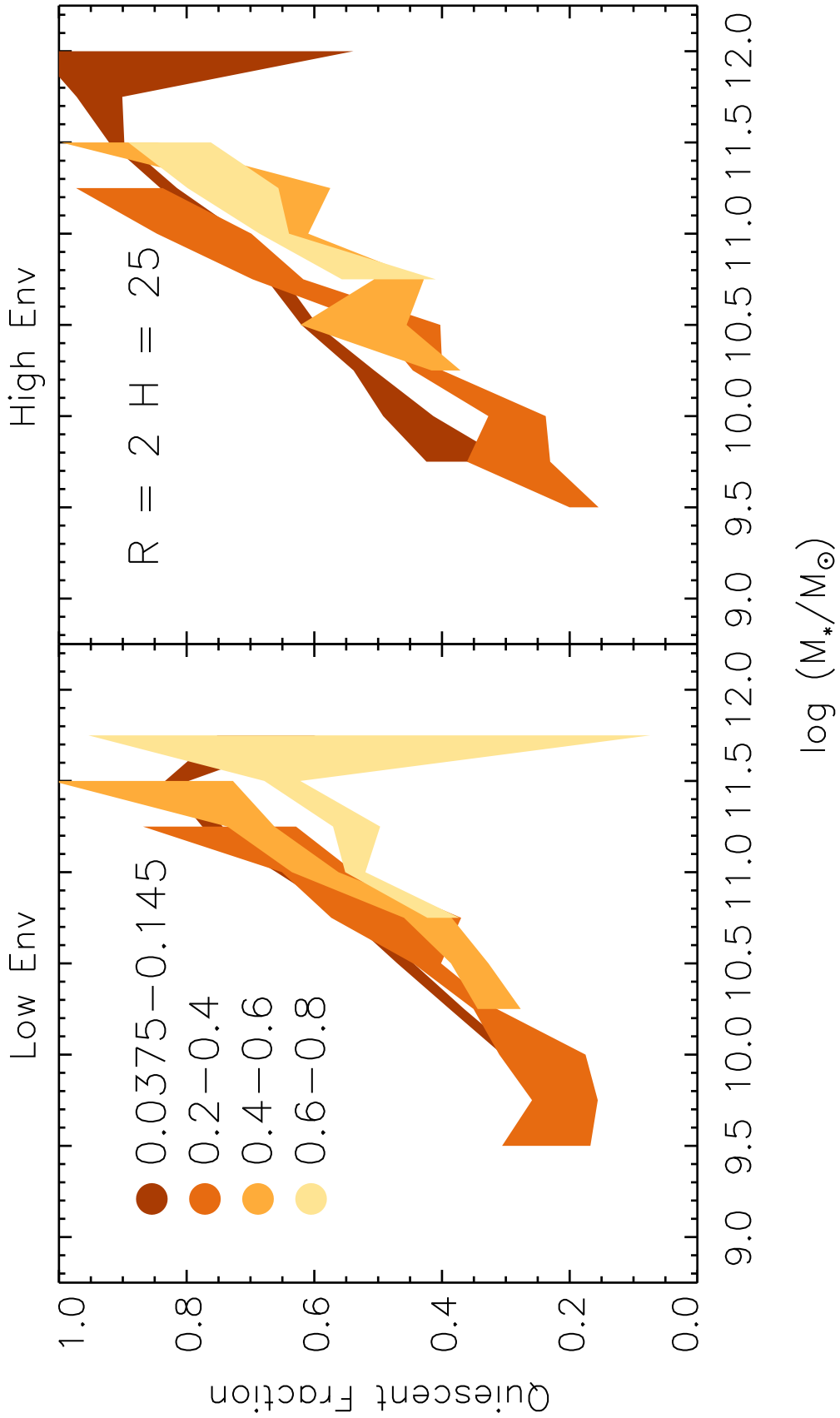
FIG. 3.— Evolution of the quiescent fraction f_Q for target galaxies in spare (left) and dense (rights) environments from $z \sim 0.7$ to $z \sim 0.1$. f_Qs were calculated using the SMFs computed in Section 3 and shown in Figure2, as described in text. Darker shading indicates lower redshift.

the survey geometry.

In order to account for these edge effects, we use a Monte Carlo method to impose edge cuts on the target galaxy population. We begin by computing the angular separation, θ_{ap} that corresponds to the radius of the aperture at the redshifts of the target galaxies. Then the galaxies are matched to a sample of $N_{ransack} = 1,000,000$ points with RA and Dec randomly generated within the window function of the EDP. We refer to this randomly generated redshift-less sample as the "ransack" sample, based on the procedure used to construct them. For each target galaxy, we count the number of ransack points, $n_{ransack}$, within θ_{ap} of the galaxy's RA and Dec value. The $n_{ransack}$ values are then compared to the expected value:

$$E[n_{ransack}] = \frac{N_{ransack}}{A_{EDP}} \times \pi\theta_{ap}^2 \times f_{thresh} \qquad (3)$$

where A_{EDP} is the total angular area of the target fields and f_{thresh} is the fractional threshold for the edge effect cut-off, which we vary based on R_{ap} (listed in Table 2). If $n_{ransack}$ for a target galaxy is greater than $E[n_{ransack}]$ then the target galaxy remains in the sample; otherwise, it is discarded from the sample.

3. STELLAR MASS FUNCTION

The target galaxy sample defined above has so far been classified into quiescent or star-forming and dense or sparse. We further divide these subsamples into bins of redshift: $0.0375-0.145$, $0.2-0.4$, $0.4-0.6$, and $0.6-0.8$. While the PRIMUS data ranges from $0.2 < z < 1.2$, we only consider galaxies with $z < 0.8$ due to insufficient statistics for robust environment measurements at $z > 0.8$. With added redshift bins, we have a total of 16 subsamples. We calculate the SMF for each of these 16 subsamples.

To calculate the SMFs we employ a non-parametric $1/V_{max}$ estimator commonly used for galaxy luminosity functions and stellar mass functions , as done in Moustakas et al. (2013b) and discussed in the review Johnston (2011). The differential SMF is given by the following equation:

$$\Phi(\log \mathcal{M})\Delta(\log \mathcal{M}) = \sum_{i=1}^{N} \frac{w_i}{V_{max,avail,i}}. \qquad (4)$$

The equation above is same as Equation 3. in Moustakas et al. (2013b) except for the distinction that we use $V_{max,avail}$ instead than V_{max}, to account for the edge effects of the survey for our environment measurements. w_i here represents the statistical weight of each galaxy i and $\Phi(\log \mathcal{M})\Delta(\log \mathcal{M})$ is the number of galaxies (N) per unit volume within the stellar mass range $[\log \mathcal{M}, \log \mathcal{M} + \Delta(\log \mathcal{M})]$.

$V_{max,i}$ is the maximum cosmological volume where it is possible to observe galaxy i given the apparent magnitude limits of the survey. However in Section 2.6 we remove the galaxies that lie on the edge from our sample. In doing so we reduce the maximum cosmological volume where a galaxy can be observed, thereby reducing $V_{max,i}$.

To calculate $V_{max,avail,i}$, we generate a sample of points with random RA, Dec within the window function of the target sample and z in the redshift range. This is not to be confused with the ransack sample in Section 2.6. We

then impose the same edge cuts we applied to the target galaxy population. At redshift bins of $\Delta z \sim 0.01$, we compute theraction of random points that remain in the bin after the edge cuts: f_{edge}. Afterwards we apply this factor to compute $V_{max,avail} = V_{max} \times f_{edge}$. The V_{max} in the equation above are computed following the method described in Moustakas et al. (2013b) Section 4.2 with the same redshift-dependent K-correction from observed SED and luminosity evolution model.

In order to calculate the uncertainty of the SMFs from the sample variance, we use a standard jackknife technique as done in Moustakas et al. (2013b). For the PRIMUS target galaxies, we calculate SMFs after excluding one of the five target fields each time. And for the SDSS target galaxies we divide the field into a 30×20 rectangular RA and Dec grid and calculate the SMFs after excluding part of the field each time. Then using the calculated SMFs we calculate the uncertainty:

$$\sigma^j = \sqrt{\frac{M-1}{M} \sum_{k=1}^{M} (\Phi_k^j - \langle\Phi^j\rangle)^2} \qquad (5)$$

M in this equation is the number of jack knife SMFs in the stellar mass bins. $\langle\Phi^j\rangle$ is the mean number density of galaxies in each stellar mass bin for all of the jack knife Φ^js.

SMFs for 16 target galaxy subsamples classified into quiescent/star-forming (orange/blue)and dense/spare environments are presented in Figure 2. The redshift evolution of the SMFs are indicated by a darker shade for lower redshifts. The sample variance uncertainties are represented by the width of the SMFs. The environment measurements and classifications for Figure 2 are done using a cylindrical aperture with dimensions, $R_{ap} = 2$ Mpc/h and $H_{ap} = 25$ Mpc/h.

Examining the SMF evolution from $z \sim 0.7$ to $z \sim 0.1$, we find that in dense environments both the star-forming and quiescent SMFs increase at $\mathcal{M}_*$ below the knee of mass function ($\log \mathcal{M}_*/\mathcal{M}_\odot < 10.75$ for star-forming; $\log\mathcal{M}_*/\mathcal{M}_\odot < 11.0$ for quiescent). Meanwhile, at masses above the knee the SMFs for dense environments exhibit little change throughout the redshift range.

At sparse environments, the quiescent SMF remains relatively constant for galaxies with $\log \mathcal{M}_*/\mathcal{M}_\odot < 10.75$. At higher stellar masses, however, the SMF decreases notably. Finally the sparse environment star-forming SMF shows a decrease at all stellar mass ranges over the redshift range.

4. QUIESCENT FRACTION

The SMFs calculated in the previous section describe the distribution of our galaxy population in stellar mass and reveal the evolution of this distribution over comic time. From the SMFs, we compute the quiescent fractions in order to compare the quiescent and the star-forming populations and to quantify the fraction of galaxies that have depleted their star-formation. Furthermore, by dividing our galaxy sample using environment measurements into dense and sparse samples, we investigate the environment dependence on the quiescent fraction and consequently on environment dependent quenching mechanisms.
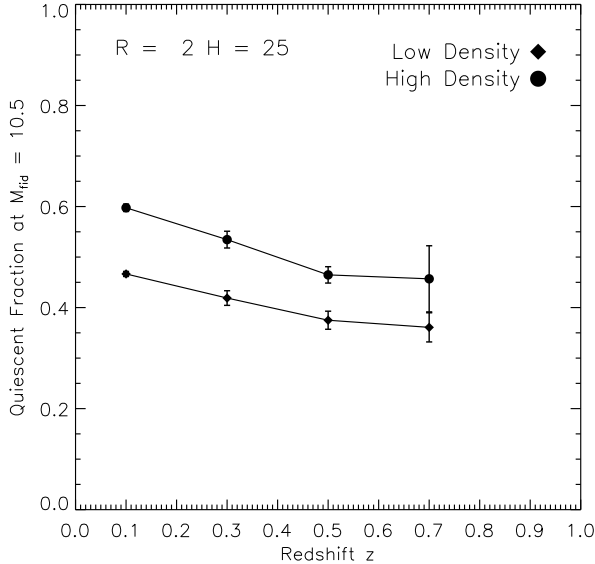
From the SMF number densities (Φ) in the previous

FIG. 4.— The evolution of the quiescent fraction at fiducial mass, $f_Q(\mathcal{M}_{\rm fid} = 10^{10.5}\mathcal{M}_\odot)$, for sparse (square) and dense (circle) environments within the redshift range $z = 0.0 - 0.8$. There is a significant increase in $f_Q(\mathcal{M}_{\rm fid})$ with decrease in redshift for both environments. In addition, over the entire redshift range, $f_Q(\mathcal{M}_{\rm fid})$ for dense environment is greater than $f_Q(\mathcal{M}_{\rm fid})$ for lower environment. However the difference in $f_Q(\mathcal{M}_{\rm fid})$ for the two environments remains constant throughout suggesting that while the quiescent fraction is higher in dense environments, the evolution of the quiescent fraction is independent of environment.

section, the quiescent fraction is computed as follows,

$$f_Q = \frac{\Phi_Q}{\Phi_{SF} + \Phi_Q}. \qquad (6)$$

Φ_Q and Φ_{SF} are the total number of galaxies per unit volume in stellar mass bin of $\Delta(\log\mathcal{M}) = 0.25$ for the quiescent and star-forming subsamples, respectively (Equation 4). We compute f_Q for dense and spare environments over our redshift range as plotted in Figure 3, which shows the evolution of f_Q for dense (right) and sparse (left) environments. As in Figure 2, the darker shading represent lower redshifts.

In both sparse and dense environments, Figure 3 clearly shows an increase in f_Q with decrease in redshift at all stellar masses. Qualitatively, this f_Q evolution exhibits a notable mass dependence. More specifically, the f_Q in sparse environments shows a greater evolution between redshift bins at high masses than at low masses. On the other hand, the f_Q in dense environments shows a greater evolution between redshift bins at low masses than at high masses.

While trends are apparent from Figure 3, quantitative comparisons of the f_Q for different environment over redshift is made challenging by the distinct stellar mass completeness limits for each redshift bin. In order to quantify the quiescent fraction over the stellar mass complete rate, we fit each f_Q to a power-law parameterization as a function of stellar mass,

$$f_Q(\mathcal{M}_*) = a \log\left(\frac{\mathcal{M}_*}{10^{10.5}\,\mathcal{M}_\odot}\right) + b, \qquad (7)$$

where a are b are best-fit parameters using *MPFIT* (**?**). The value $10^{10.5}\,\mathcal{M}_\odot$ in the equation represents an empirically selected fiducial mass $\mathcal{M}_{\rm fid}$ within the stellar mass completeness limits. This fiducial mass serves to highlight and quantify the f_Q evolution for different redshifts and using $\mathcal{M}_{\rm fid} = 10^{11}\mathcal{M}_\odot$ does not notably alter the results. Figure 4 shows the evolution of $f_Q(\mathcal{M}_{\rm fid})$ from $z \sim 0.7$ to ~ 0.1 for sparse (diamond) and dense (circle) environments. For both dense and spare environments, $f_Q(\mathcal{M}_{\rm fid})$ increases as redshift decreases. In addition, through the redshift range explored in our analysis, dense environment $f_Q(\mathcal{M}_{\rm fid})$ is significantly greater than the sparse environment $f_Q(\mathcal{M}_{\rm fid})$. However when we compute $f_Q(\mathcal{M}_{\rm fid})_{\rm dense} - f_Q(\mathcal{M}_{\rm fid})_{\rm sparse}$, we find the difference remains constant throughout the redshift range (< 0.15 throughout redshift range). Furthermore, the total evolution of $f_Q(\mathcal{M}_{\rm fid})$ from $z \sim 0.7$ to ~ 0.1 show no strong environment dependence.

The analysis described in this paper use a fixed cylindrical aperture with dimensions $R_{\rm ap} = 2$ Mpc and $H_{\rm ap} = 25$ Mpc to measure environment, the same analysis was extended for varying aperture dimensions $R_{\rm ap} = 1, 2, 3$ Mpc and $H_{\rm ap} = 25, 50$ Mpc. Minor adjustments to the environment classification thresholds were adopted in these analyses for the smaller apertures ($r_{\rm ap} = 0.5, 1$Mpc and $r_{\rm ap} = 25$Mpc). The results obtained from using these different are consistent with the results displayed in this paper.

5. SUMMARY

We have measured the SMFs and QFs using low redshift SDSS-*GALEX* galaxies and intermeidate redshift PRIMUS galaxies. Specifically we anlayzed the evolution of the QFs over the redshift range $0.0 - 1.0$ for galaxies in environment densities (Figure 3). We find that there is an expected increase in QF with decrease in the redshift for subsamples in all environment densities. More importantly we find that the change in QF over redshift is independent of the environment and remains relatively equal for all environments.

- Comparison to other works.

  – Alberts et al. 2013

REFERENCES

Abazajian, K. N., Adelman-McCarthy, J. K., Agüeros, M. A., et al. 2009, ApJS, 182, 543
Baldry, I. K., Glazebrook, K., & Driver, S. P. 2008, MNRAS, 388, 945
Behroozi, P. S., Marchesini, D., Wechsler, R. H., et al. 2013, ApJ, 777, L10
Bell, E. F., Papovich, C., Wolf, C., et al. 2005, ApJ, 625, 23

Blanton, M. R., Eisenstein, D., Hogg, D. W., & Zehavi, I. 2006, ApJ, 645, 977
Blanton, M. R., Lupton, R. H., Schlegel, D. J., et al. 2005a, ApJ, 631, 208
Blanton, M. R., & Moustakas, J. 2009, ARA&A, 47, 159
Blanton, M. R., Schlegel, D. J., Strauss, M. A., et al. 2005b, AJ, 129, 2562

TABLE 2
Fixed Cylindrical Aperture Dimensions

Radius (Mpc)	Height (Mpc)	n_{bin}	Edgecut	High Env Threshold (galaxies)	Low Env Threshold (galaxies)
1.0	50	6	80%	1.5	0.0
2.0	50	6	75%	4.0	0.0

Borch, A., Meisenheimer, K., Bell, E. F., et al. 2006, A&A, 453, 869
Bundy, K., Ellis, R. S., Conselice, C. J., et al. 2006, ApJ, 651, 120
Chabrier, G. 2003, PASP, 115, 763
Coil, A. L., Blanton, M. R., Burles, S. M., et al. 2011, ApJ, 741, 8
Colless, M., Dalton, G., Maddox, S., et al. 2003, VizieR Online Data Catalog, 7226, 0
Conroy, C., & Gunn, J. E. 2010, FSPS: Flexible Stellar Population Synthesis, astrophysics Source Code Library, ascl:1010.043
Cool, R. J., Moustakas, J., Blanton, M. R., et al. 2013, ApJ, 767, 118
Cooper, M. C., Newman, J. A., Weiner, B. J., et al. 2008, MNRAS, 383, 1058
Croton, D. J., Farrar, G. R., Norberg, P., et al. 2005, MNRAS, 356, 1155
Desai, V., Dalcanton, J. J., Aragón-Salamanca, A., et al. 2007, ApJ, 660, 1151
Dressler, A. 1980, ApJ, 236, 351
Dressler, A. 1984, ARA&A, 22, 185
Geha, M., Blanton, M. R., Yan, R., & Tinker, J. L. 2012, ApJ, 757, 85
Guillaume, M., Llebaria, A., Aymeric, D., Arnouts, S., & Milliard, B. 2006, in Society of Photo-Optical Instrumentation Engineers (SPIE) Conference Series, Vol. 6064, Image Processing: Algorithms and Systems, Neural Networks, and Machine Learning, ed. E. R. Dougherty, J. T. Astola, K. O. Egiazarian, N. M. Nasrabadi, & S. A. Rizvi, 332–341
Guzzo, L., Strauss, M. A., Fisher, K. B., Giovanelli, R., & Haynes, M. P. 1997, ApJ, 489, 37
Hermit, S., Santiago, B. X., Lahav, O., et al. 1996, MNRAS, 283, 709

Hopkins, A. M., & Beacom, J. F. 2006, ApJ, 651, 142
Hubble, E. P. 1936, The Realm of the Nebulae (New Haven: Yale University Press)
Jarrett, T. H., Chester, T., Cutri, R., et al. 2000, AJ, 119, 2498
Johnston, R. 2011, A&A Rev., 19, 41
Kovač, K., Lilly, S. J., Knobel, C., et al. 2010, ApJ, 718, 86
Leja, J., van Dokkum, P., & Franx, M. 2013, ApJ, 766, 33
Magnelli, B., Elbaz, D., Chary, R. R., et al. 2009, A&A, 496, 57
Martin, D. C., Fanson, J., Schiminovich, D., et al. 2005, ApJ, 619, L1
Morrissey, P., Schiminovich, D., Barlow, T. A., et al. 2005, ApJ, 619, L7
Moustakas, J., Coil, A. L., Aird, J., et al. 2013a, ApJ, 767, 50
—. 2013b, ApJ, 767, 50
Muldrew, S. I., Croton, D. J., Skibba, R. A., et al. 2012, MNRAS, 419, 2670
Noeske, K. G., Weiner, B. J., Faber, S. M., et al. 2007, ApJ, 660, L43
Oemler, A. 1974, ApJ, 194, 1
Patel, S. G., Holden, B. P., Kelson, D. D., Illingworth, G. D., & Franx, M. 2009, ApJ, 705, L67
Pozzetti, L., Bolzonella, M., Zucca, E., et al. 2010, A&A, 523, A13
Salim, S., Rich, R. M., Charlot, S., et al. 2007, ApJS, 173, 267
Springel, V., White, S. D. M., Jenkins, A., et al. 2005, Nature, 435, 629
Taylor, E. N., Franx, M., van Dokkum, P. G., et al. 2009, ApJ, 694, 1171

APPENDIX

Stellar Mass Function

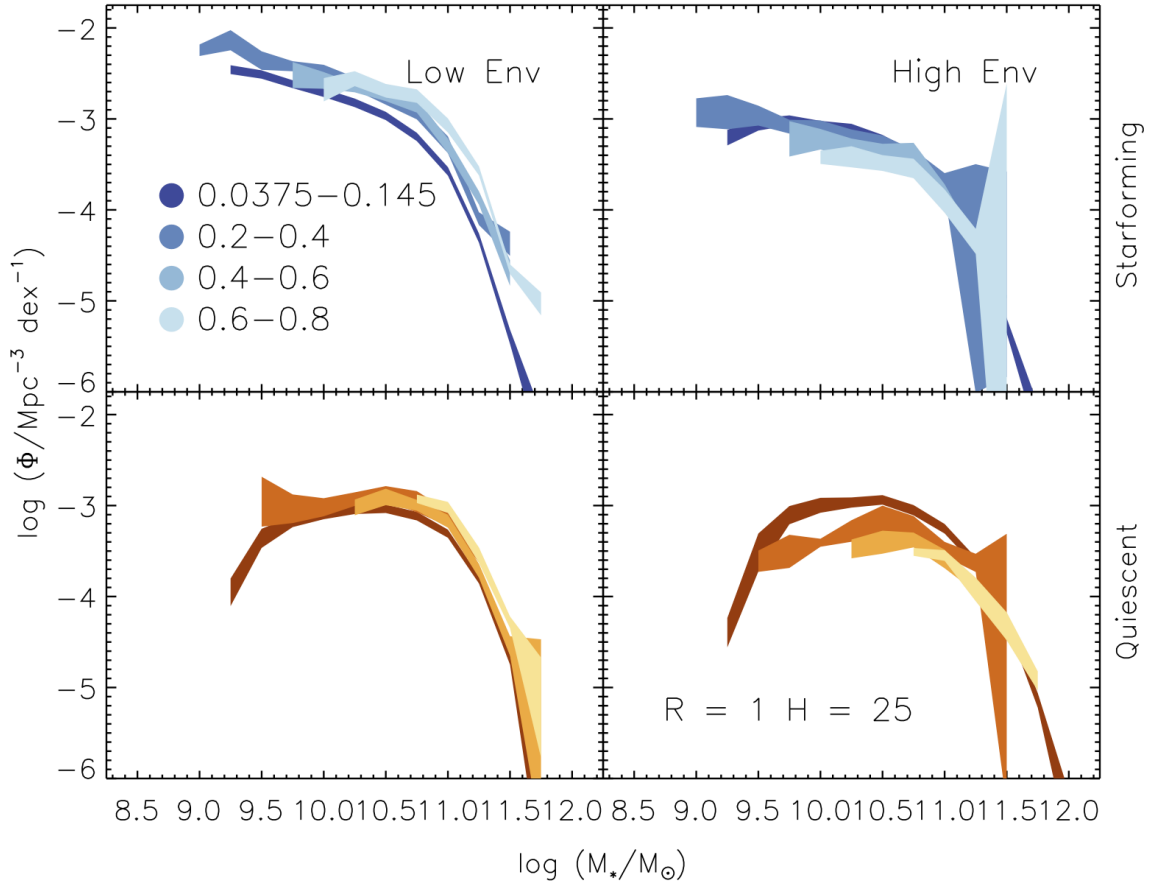FIG. 5.— SMF for $r_{\rm ap} = 1$Mpc and $h_{\rm ap} = 25$Mpc
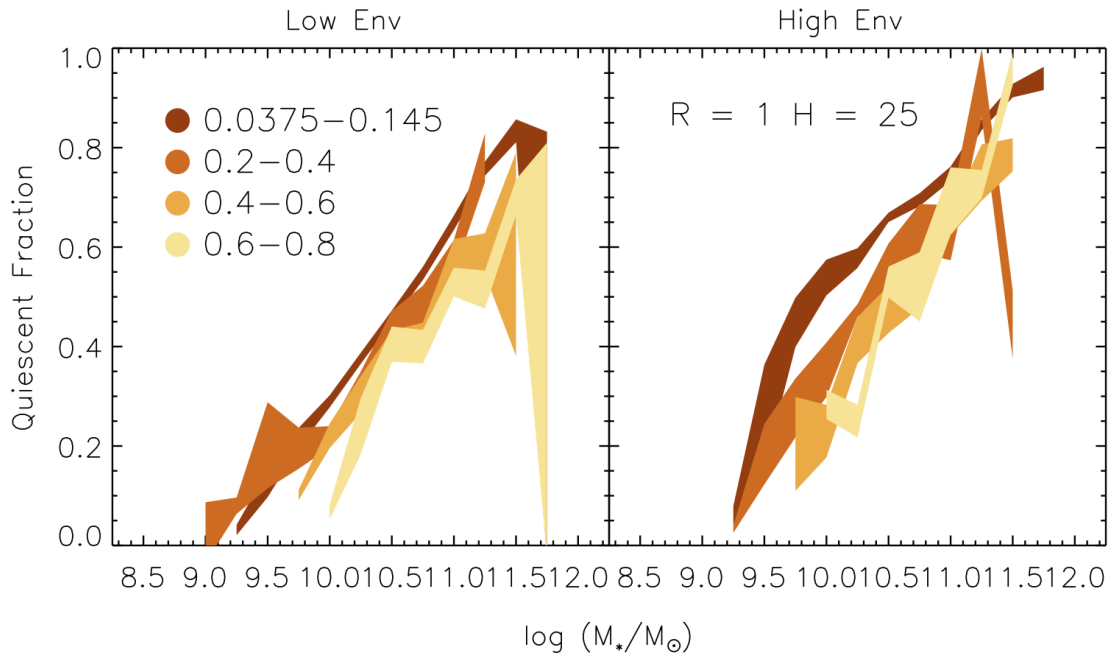
FIG. 6.— QF for $r_{\rm ap} = 1$Mpc and $h_{\rm ap} = 25$Mpc
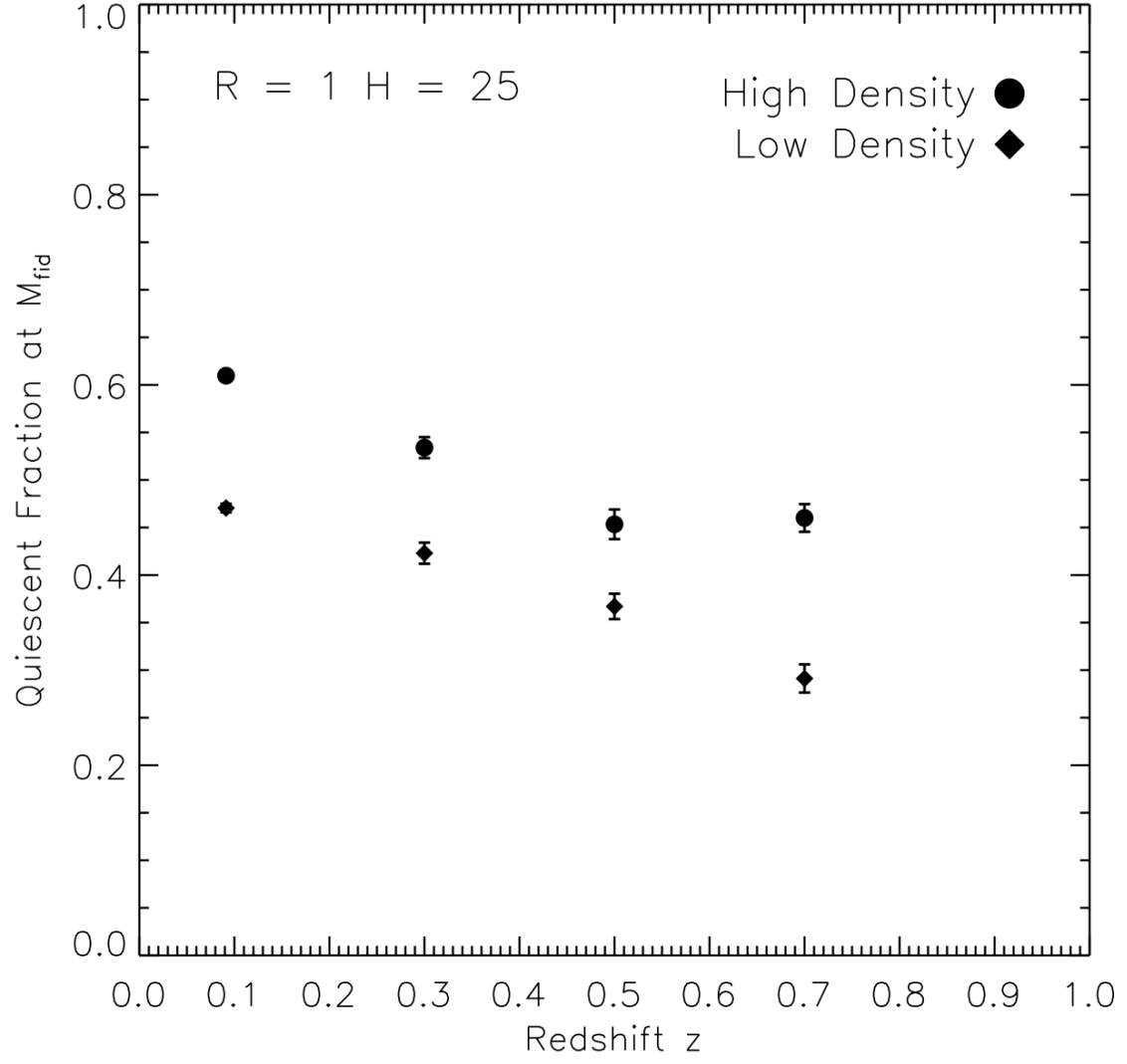
FIG. 7.— QF at fiducial mass for $r_{\mathrm{ap}} = 2\mathrm{Mpc}$ and $h_{\mathrm{ap}} = 50\mathrm{Mpc}$